Free-viewpoint images captured using phase-shifting synthetic aperture digital holography

Tatsuya Nakatsuji and Kyoji Matsushima*

Department of Electrical and Electronic Engineering, Kansai University, Yamate-cho 3-3-35, Suita, Osaka 564-8680, Japan

*Corresponding author: matsu@kansai-u.ac.jp

Free-viewpoint images obtained from phase-shifting synthetic aperture digital holography are given for scenes that include multiple objects and a concave object. The synthetic aperture technique is used to enlarge the effective sensor size and to make it possible to widen the range of changing perspective in the numerical reconstruction. The lensless Fourier setup and its aliasing-free zone are used to avoid aliasing errors arising at the sensor edge and to overcome a common problem in digital holography, namely, a narrow field of view. A change of viewpoint is realized by a double numerical propagation and by clipping the wave field by a given pupil. The computational complexity for calculating an image in the given perspective from the base complex-valued image is estimated at a double fast Fourier transform. The experimental results illustrate the natural change of appearance in cases of both multiple objects and a concave object. © 2008 Optical Society of America

OCIS codes: 090.1995, 110.6880.

1. Introduction

The explosive evolution of computer technology has increasingly accelerated digital signal processing (DSP) in the field of optics. A great deal of memory is required for handling light wave fields correctly. However, the amount of memory installed in personal computers increases from year to year, with the result that desktop computers with high-performance CPUs and gigabytes of memory enable us to handle wave fields sampled over a certain area of the cross section of field propagation.

This yields the possibility that various effects for wave fields, created by optical components such as lenses, mirrors, prisms, or specific optical devices, can be replaced by DSP. Digital holography provides an acquisition system of wave fields emitted from real objects and is therefore the most important technique for the DSP of light. For example, the focusing device in imaging equipment, composed of various lenses controlled mechanically, can be replaced by DSP. As a further example, images on planes that are almost perpendicular to the image sensor can be clearly reconstructed by using a specific computational process of captured wave fields [1].

As the phase distribution of object fields captured by digital holography is also useful for shape measurement and deformation analysis, much of the literature on digital holography focuses on this field, especially on holographic microscopy [2]. In this paper, however, we explore the possibility of digital holography as an acquisition method for free-viewpoint images of scenes with self- and mutual occlusion. Here, the term occlusion, widely used in the field of computer graphics and three-dimensional (3D) imaging, describes the situation in which an object further from the viewpoint is hidden behind other objects closer to the viewpoint. Occlusion is one of the most important mechanisms in the perception of 3D scenes. Free-viewpoint images of occluded objects have been reported in some methods and devices based on ray optics, such as synthetic aperture integral imaging [3,4]. As far as we know, however, the natural reconstruction of 3D scenes with occluded objects has not yet been reported in digital holography. In computer-generated holograms for display purposes, dealing with occlusion is a problem

of hidden-surface removal, and methods such as the layered hologram [5], ray tracing [6], the silhouette mask [7,8], and the tilted mask [9] have been reported. Superimposing occlusion into the wave field captured by using digital holography has also been proposed for 3D scene reconstruction [10].

The reason that natural reconstruction of occlusion is difficult in digital holography is that the resolution of image sensors currently available is too low and the sensor size too small to capture 3D scenes with occlusion. Low spatial resolution of the image sensor restricts the geometry of the object space; i. e., small objects must be placed far from the sensor to maintain the aliasing-free condition required by Nyquist's theorem. As the object distance d increases with the increasing lateral extent of the object w as shown in Fig. 1, the angle of the visual field θ is generally small in digital holography. Furthermore, a greater object distance leads to a smaller angle φ as illustrated in Fig. 1. This angle, defined by the distance d and the size of the image sensor W, is referred to as the viewing-zone angle by analogy to a 3D display. In digital holography, typical values for the visual field and viewing-zone angles are approximately ~2° and ~1°, respectively (assuming a sensor pitch of $10\,\mu m$, sensor size of $20\,mm$, and object distance of $1\,m$). Therefore, numerical reconstruction of a different perspective is not easy.

To overcome these problems and create free-viewpoint images in digital holography, we adopt three techniques: synthetic aperture [11,12], phase shifting [13], and a lensless Fourier setup [14,15]. In this investigation, the synthetic aperture technique is used to extend the effective sensor size. This technique was first proposed to improve the spatial resolution in centimeter band radars. In the same vein, superresolution has been reported when the synthetic aperture technique is used in digital holography [11,12]. However, our reason for using the technique differs from that of superresolution, and the object size captured is considerably larger than that given in previous reports.

The phase-shifting lensless Fourier setup and the aliasing-free zone presented in this paper make it possible to maximize the visual field and minimize the object distance. These techniques, which use a spherical reference wave, also play an important role in avoiding the alia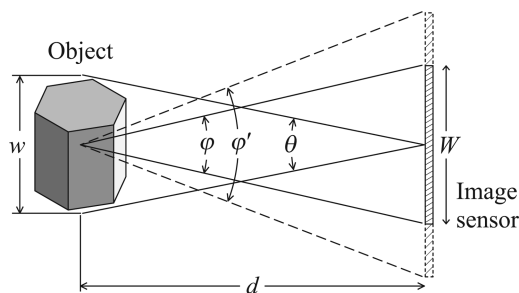sing error arising at the sensor edge, because the fringe frequency is almost constant over the sensor surface in a spherical reference wave, unlike that in a plane wave. As a result, the viewing-zone angle can be increased from φ to φ' by extending the sensor area, as shown in Fig. 1.

Our final aim is varied digital processing of optical wave fields. The wave field must be captured in a wide cross section of field propagation to accomplish this. Numerical reconstruction of free-viewpoint images is an example of the DSP of optical wave fields.

2. Reconstruction of Free-Viewpoint Images

The coordinate system defined for the numerical reconstruction of digital holograms is shown in Fig. 2. The plane $(x, y, 0)$ is referred to as the reconstruction plane on which a point light source that emits the reference wave is placed and on which wave fields are obtained. The surface of the image sensor is placed at a distance d_R from the reconstruction plane.

A. Numerical Reconstruction in a Lensless Fourier Setup

Suppose that the wave field of the object wave is given by $f(x, y, 0)$ in the reconstruction plane and $O(x_s, y_s)$ on the surface of the image sensor. When the point source is at the origin, the reference wave is represented by the normalized parabolic phase function as follows:

$$R(x_s, y_s) = \exp\left[ik\frac{x_s^2 + y_s^2}{2d_R}\right], \quad (1)$$

where $k = 2\pi/\lambda$ is the wavenumber and λ is the wavelength. The product $O(x_s, y_s)R^*(x_s, y_s)$ is captured by using a phase-shifting technique and is represented by using a Fresnel transform of $f(x, y, 0)$ as follows:

$$OR^*(x_s, y_s) = \int\int f(x, y, 0)\exp\left[i\frac{k}{2d_R}(x^2 + y^2)\right]$$
$$\times \exp\left[-i\frac{2\pi}{\lambda d_R}(xx_s + yy_s)\right]dxdy$$
$$= \mathcal{F}\{f(x, y, 0)\phi^*(x, y)\}_{u=x_s/\lambda d_R, v=y_s/\lambda d_R}, \quad (2)$$

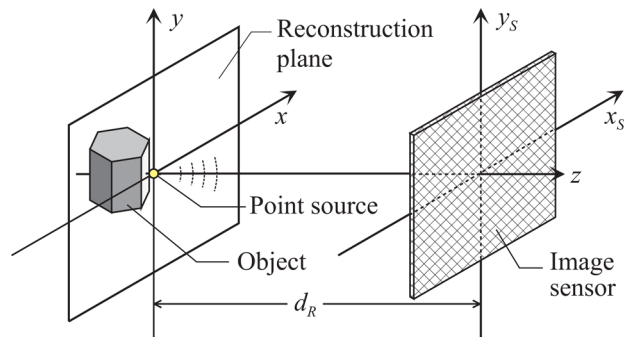Fig. 1. Definition of the visual field in capturing wave fields and the viewing zone in numerical reconstruction.

Fig. 2. (Color online) Definition of the coordinate systems and schematic geometry used in numerical reconstruction.

$$\phi(x,y) = \exp\left[-i\frac{k}{2d_R}(x^2+y^2)\right], \qquad (3)$$

where $\mathcal{F}\{\cdot\}$ represents the Fourier transform and u and v are Fourier frequencies with respect to x and y, respectively. The $\phi(x,y)$ represents a phase correction factor. The wave field of the object is obtained by rearranging Eq. (2) after the Fourier transform:

$$f(x,y,0) = \mathcal{F}\{OR^*(x_s,y_s)\}_{u_s=-x/\lambda d_R, v_s=-y/\lambda d_R} \times \phi(x,y), \qquad (4)$$

where u_s and v_s are Fourier frequencies with respect to x_s and y_s, respectively.

In the numerical calculation, the sampling pitches of the wave field $f(x,y,0)$ are given by

$$\Delta_x = \frac{\lambda d_R}{N_x \delta x}, \qquad \Delta_y = \frac{\lambda d_R}{N_y \delta y}, \qquad (5)$$

where δ_x and δ_y are the sensor pitches and N_x and N_y are the number of pixels in the sensor used for capturing the interference fringe.

B.   Numerical Reconstruction of Different Perspectives

The amplitude image $|f(x,y,0)|$ gives a reconstructed image of the object. However, the viewpoint of the object cannot be changed in the image $|f(x,y,0)|$. To give the image the ability to vary the viewpoint, the wave field $f(x,y,0)$ should be propagated numerically to a plane around the image sensor. This is the forward propagation shown in Fig. 3.

The angular spectrum of plane waves method [16] is used for this numerical propagation; i.e., the wave field in the plane at $z=d_P$ is given by

$$f(x,y,d_P) = \mathcal{P}_{d_P}\{f(x,y,0)\}$$
$$= \mathcal{F}^{-1}\{F_0(u,v)\exp[i2\pi(\lambda^{-2}-u^2-v^2)^{1/2}d_P]\}, \qquad (6)$$

where $\mathcal{P}_d\{\cdot\}$ represents the propagation operator at a distance d and $F_0(u,v) = \mathcal{F}\{f(x,y,0)\}$ is the spectrum in the reconstruction plane. Note that t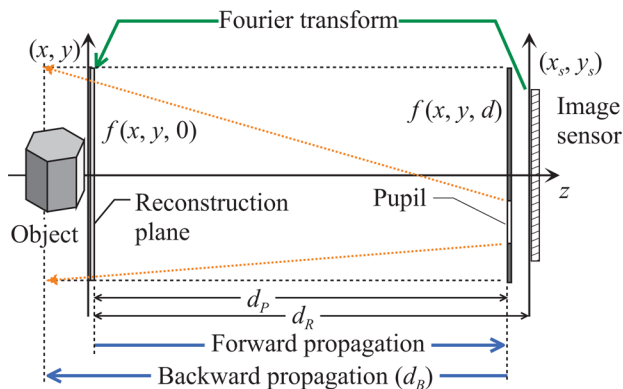he sampling pitches of the wave field are not changed in the numerical propagation by Eq. (6). Therefore, the propagation distance d_P should be selected carefully so that the extent of the wave field is not greater than the sampling area at $z = d_P$. If the distance d_P is too great, degradation arises in the final reconstructed images as a result of the aliasing error in the numerical calculation of Eq. (6).

The wave field $f(x,y,d_P)$ is the base complex-valued image for yielding a series of images of the object from different viewpoints. Changing the viewpoint is done simply by multiplying the base complex image by a pupil function as follows:

$$\hat{f}(x,y,d_P; x_e,y_e) = f(x,y,d_P)p(x,y; x_e,y_e). \qquad (7)$$

The definition of the pupil function used in this report is shown in Fig. 4. The pupil is a rectangle pupil, the size and position of which are given by $p_x \times p_y$ and (x_e, y_e), respectively.

The wave field $\hat{f}(x,y,d_P; x_e,y_e)$ clipped by the pupil is propagated backward as follows:

$$\hat{f}(x,y,0; x_e,y_e) = \mathcal{P}_{-d_B}\{\hat{f}(x,y,d_P; x_e,y_e)\}, \qquad (8)$$

where $d_B(\geq 0)$ is the distance of backward propagation chosen to adjust the focus. The amplitude image $|\hat{f}(x,y,d_P-d_B; x_e,y_e)|$ is the final image from the viewpoint at (x_e,y_e,d_P).

3.   Capturing Object Waves

A.   Experimental Setup

The lensless Fourier setup in synthetic aperture digital holography is shown in Fig. 5. The output of the single-mode diode-pumped solid-state laser with a wavelength of 532 nm is split into two paths. The piezo phase shifter and the spatial filter are inserted into the reference path to form a phase controlled spherical reference wave. Here, d_R is the distance between the reference point source and the image sensor, as defined in Fig. 2. The object is also irradiated by a spherical wave formed by the objective lens. The object wave and the reference wave are combined in the cube beam splitter and yield an interference

Fig. 3.   (Color online) Principle of numerical reconstruction from different viewpoints.
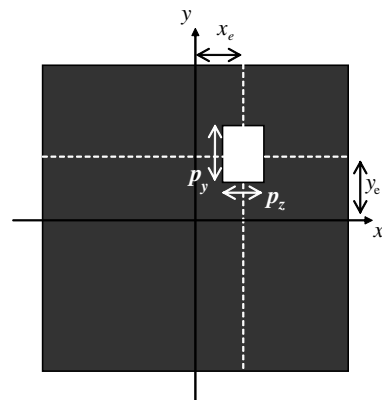

Fig. 4.   Definition of a pupil.

fringe on the sensor surface. A CMOS-type image sensor is used to capture the fringe pattern. The number of pixels in the image sensor is 2000 × 2000 pixels, and its sampling pitch is $6.0\,\mu m \times 6.0\,\mu m$.

As the image sensor is moved translationally in this experiment, instead of rotating the object as in [11], the sensor is installed on a motor-controlled translational stage, and its position is shifted perpendicular to the optical axis. The resolution and accuracy of the motor-controlled stage are 2 and $15\,\mu m$, respectively. The distribution of the complex amplitude is obtained by a four-step phase shift in this experiment. Four fringe patterns are therefore captured for each position of the sensor, and then a complex-valued image is composed of these captured fringe patterns by using the phase-shifting digital holography technique [13].

B. Aliasing-Free Zone

To maximize the visual field in the lensless Fourier setup, we use a technique referred to as the aliasing-free zone. The aliasing-free zone is a safe zone defined in the object space. When an object placed inside the aliasing-free zone is captured by the lensless Fourier setup, the reconstructed images are not degraded by the aliasing error.

The maximum fringe frequency should be estimated in a lensless Fourier setup to define the aliasing free-zone. Figure 6 shows the theoretical model used in the estimation. For simplicity, we ignore the y axis and consider the 2D coordinates (x, z) in the estimation that follows. Furthermore, it is assumed that the point object P is on the same plane as the reference point source R and placed at a distance $w/2$ from the optical axis. When point S is on the sensor surface and $\Delta\theta$ is the angle between line segments PS and RS, the wavelength of the fringe caused by the interference between the point sources P and R is given as

$$\Lambda = \frac{2\pi}{|k_P - k_R|}, \qquad (9)$$

where k_P and k_R are x elements of the wave vectors of fields propagating from the point sources P and R to the point S, respectively.
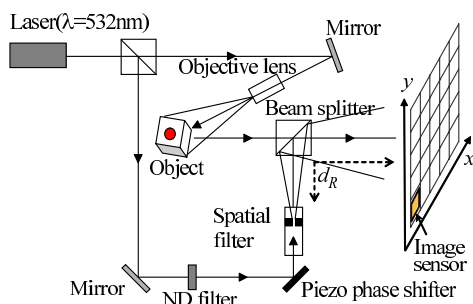
Fig. 5. (Color online) Experimental setup for capturing object waves by phase-shifting synthetic aperture digital holography.
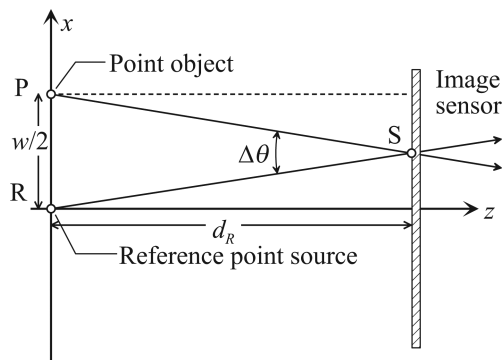
Fig. 6. Theoretical model for estimating the maximum spatial frequency of the interference fringe on the sensor surface.

Obviously, the interference fringe has a maximum frequency when the angle $\Delta\theta$ is at its maximum. When the point S is at the position $x = w/4$, $\Delta\theta$ reaches the maximum angle. In this case, since $k_R = -k_P = \sin(\Delta\theta/2)$, the minimum value of the fringe wavelength is given by

$$\Lambda_{\min} = \frac{\lambda}{2\sin(\Delta\theta/2)}, \qquad (10)$$

where $\sin(\Delta\theta/2)$ is given by the geometry as follows:

$$\sin(\Delta\theta/2) = \frac{w/4}{\sqrt{d^2 + (w/4)^2}}. \qquad (11)$$

To avoid aliasing errors, the sensor pitch δ must satisfy Nyquist's condition $2\Lambda_{\min}^{-1} \le \delta^{-1}$. As a result, the object size w must be limited as follows:

$$w \le \frac{4\lambda d}{\sqrt{16\delta^2 - \lambda^2}}. \qquad (12)$$

If the size of an object placed at a distance d is less than w given by the above relation, aliasing errors do not arise. Therefore, the zone fulfilling condition (12) is referred to as the aliasing-free zone. This zone is shaped as a triangular pyramid in the object space as shown in Fig. 7. We can obtain a maximum visual field by placing an object inside the aliasing-free zone and minimizing the distance from the image sensor for the given object.
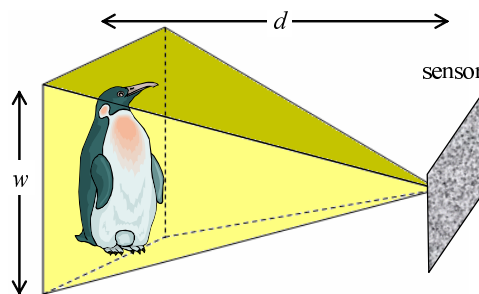
Fig. 7. (Color online) Aliasing-free zone.

4. Experimental Results

A. Calibration of the Distance of the Reference Point Source

A fairly large object was captured by the lensless Fourier setup without the synthetic aperture technique in order to verify the visual field of the constructed capturing system. An example of the amplitude image $|f(x,y,0)|$ is shown in Fig. 8. The dimension of the object is $3\,\text{cm} \times 4.5\,\text{cm}$. Since the aliasing-free zone is given by $w \leq 0.089d$ in the experimental setup, the minimum object distance is $50\,\text{cm}$. Therefore, the object was placed at approximately $60\,\text{cm}$ from the sensor to allow for a margin of error.

The distance between the reference point source and the image sensor d_R affects both the sampling pitch of the wave field in Eq. (5) and the phase correction factor in Eq. (3). Since the precision of numerical propagation is strongly affected by both, the accuracy of d_R is important. If d_R is not accurate, a clear final image cannot be obtained from the proposed method, because numerical propagation is used twice for generating the image from a given viewpoint. We calibrated d_R by exact comparison between the dimension of the actual object and the extent of the object on the reconstructed amplitude image $|f(x,y,0)|$. Exact sampling pitches are measured first by the comparison, and then an exact d_R is obtained from Eq. (5). Once the distance d_R is calibrated, it is no problem to replace and shift the object within a certain range. In the results from Fig. 8, the calibrated distance d_R and sampling pitch of the wave field $f(x,y,0)$ are $61.7\,\text{cm}$ and $26.7\,\mu\text{m}$, respectively.

An example of an amplitude image $|f(x,y,d_P)|$ of the propagated wave field is shown in Fig. 9. Here, the calibrated distance and the sampling pitches are $61.9\,\text{cm}$ and $26.8\,\mu\text{m}$, respectively. Figure 10 shows the geometry of the object. Since the reconstruction plane coincides with the plane of the letter "K," no numerical propagation is required for reconstruction in Fig. 9(a), whereas the wave field is propagated to the plane at $d_P = -6.0\,\text{cm}$ in Fig. 9(b).
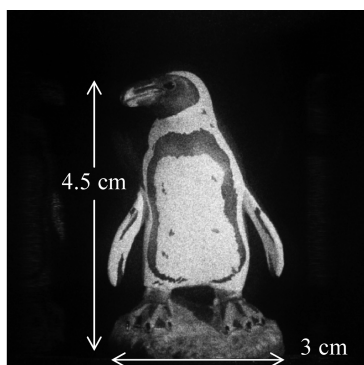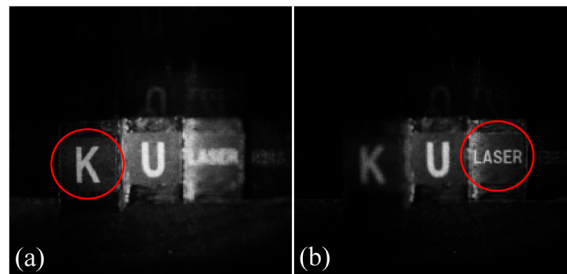

Fig. 9. (Color online) Numerical reconstruction without synthetic aperture technique. The amplitude image of the wave field (a) without and (b) with numerical propagation. The propagation distance is $d_P = -6.0\,\text{cm}$. Each image contains 2048×2048 pixels.

Clear images are reconstructed by accurate numerical propagation.

B. Stitching Complex-Valued Images

Multiple complex-valued images captured by using the phase-shifting technique are stitched up and combined into a large complex-valued image. Figure 11 is an example of a stitched complex-valued image composed of 5×5 segments. The number of pixels of the individual segments is approximately 1330×1330 pixels. This segment size is smaller than the sensor size, because all segments are captured at intervals less than the sensor size to give an overlap between adjacent segments and enable them to be stitched exactly. The correlation function is calculated for each pair of adjacent segments to detect the exact overlap position [11]. The positioning error of the motor-controlled stage, obtained from the correlation function, is approximately $40\,\mu\text{m}$.

C. Reconstructed Images from Different Viewpoints

Examples of amplitude images $|\hat{f}(x,y,0;x_e,y_e)|$ reconstructed from different viewpoints are shown in Fig. 12. The object is a nut. The stitched complex-valued image with the number of samplings 7346×7334 is embedded in 8192×8192 sampling grids to perform the fast Fourier transform. The calibrated distance d_R is $18.6\,\text{cm}$, and thus the pixel pitch of

Fig. 8. Numerical reconstruction without numerical propagation and the synthetic aperture technique. The number of pixels is 2048×2048 pixels.
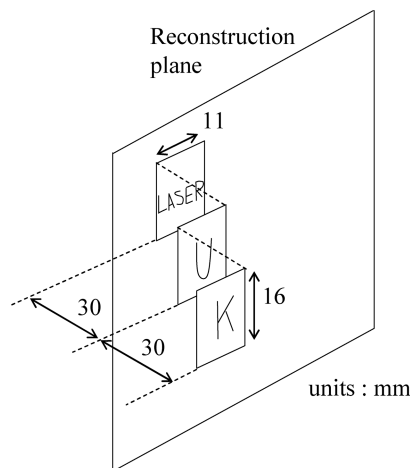

Fig. 10. Schematic geometry of the object reconstructed in Fig. 9.
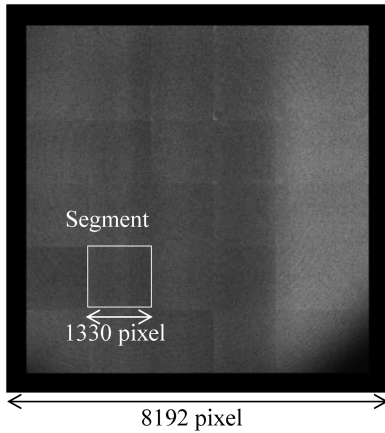
Fig. 11. Example of a synthetic complex-valued image stitched from 5 × 5 segments.

Fig. 13. (Multimedia online; ao.osa.org) Amplitude images $|f(x, y, -3.0\,\mathrm{cm}; x_e, y_e)|$ of mutually occluded objects from different viewpoints (associated movie file, 1.0 Mbyte).

the wave field $f(x, y, 0)$ after the fast Fourier transform is $2.01\,\mu\mathrm{m}$. The wave field is again embedded in $32,768 \times 32,768$ sampling grids to avoid any aliasing errors in the numerical propagation and then propagated forward to a plane at a distance $d_P = 20\,\mathrm{cm}$ from the reconstruction plane. The propagated wave field is masked by a pupil aperture with dimensions $3.2 \times 3.2\,\mathrm{mm}$ and then propagated backward to the reconstruction plane. Finally, the region containing the object is clipped from the wave field.

Amplitude images reconstructed from different perspectives are shown in Fig. 12. Viewpoints of the image move from left ($x_e = -16.5\,\mathrm{mm}$) in Fig. 12(a) to right ($x_e = +16.5\,\mathrm{mm}$) in Fig. 12(c). The change of degree of self-occlusion is observed in the toruslike shape of the nut. A multimedia file is provided to demonstrate the free-viewpoint reconstruction.

Other examples of the numerical reconstruction of multiple objects with mutual occlusion and the geometry of the objects are shown in Figs. 13 and 14, respectively. Almost all the parameters for capturing and reconstructing are the same as those in Fig. 12, but the viewpoint moves vertically in 13(a) and 13(c) as well as horizontally in 13(a) and 13(b). The change in occlusion is demonstrated more clearly than in Fig. 12, because mutual occlusion occurs in this example. The pips of the six pattern on a die are all hidden behind another die in 13(a) and partially hidden in 13(c), while all of the pattern is clearly shown

in 13(b) and 13(d). A multimedia file demonstrating this change in viewpoint is also provided.

5. Discussion

Numerical reconstruction of different perspectives is dependent not only on the viewpoint (x_e, y_e), but also on the pupil size $p_x \times p_y$ and distance d_P. The pupil size gives the depth of focus of the reconstructed images. A smaller pupil gives a deeper depth of focus, but this most likely causes speckle problems. Amplitude images reconstructed for different pupil sizes are shown in Figs. 16(a)–16(c) below. Speckle noise increases significantly with decreasing pupil size. This is one of the well-known properties of image formation from coherent light.

The depth of focus is actually given by angles $\Delta\varphi_{x,y} \approx p_{x,y}/d_P$ rather than the pupil size itself, as shown in Fig. 15(a). When a pupil is placed at a distance d'_P in the line of sight and the size is given as

$$p'_x \times p'_y = (p_x \times p_y) d'^2_P / d^2_P, \qquad (13)$$

the pupil seems to play the same role as the pupil at the distance d_P. However, this causes the problem of narrowing the visual field. Amplitude images reconstructed with pupils at different distances, but in the same line of sight, are shown in Figs. 16(d)–16(f). The appearance of the object does not change noticeably, but the visual field decreases as the pupil distance d_P decreases. Furthermore, in the case of a small dis-
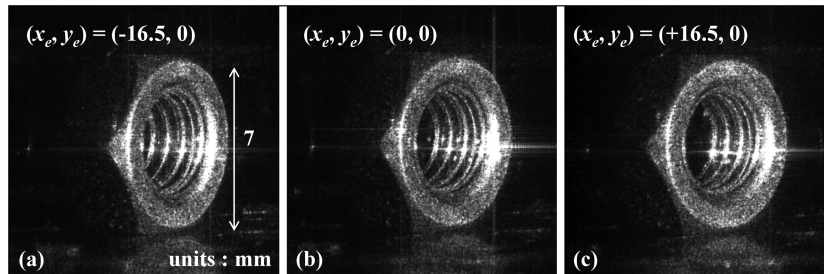

Fig. 12. (Multimedia online; ao.osa.org) Amplitude images $|f(x, y, 0; x_e, y_e)|$ of a self-occluded object from different viewpoints (associated movie file, 499 Kbytes).
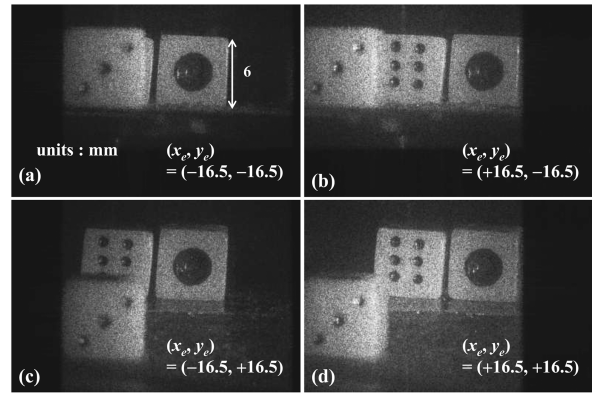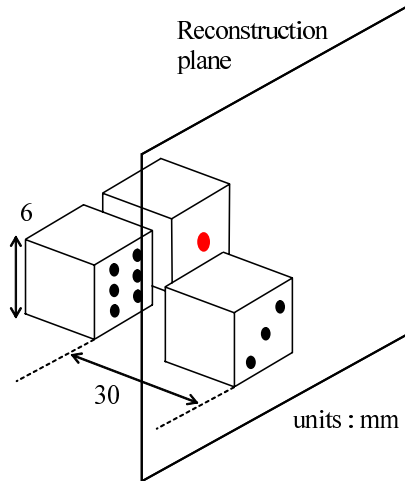
Fig. 14. (Color online) Schematic geometry of the mutually occluded objects reconstructed in Fig. 13.

Fig. 15. (Color online) Visual field in the numerical reconstruction from different viewpoints.

tance as in Fig. 16(f), the image is degraded because of the small number of sampling points within the pupil.

The entire object can be reconstructed if the whole object field reaches the pupil. This is illustrated in Fig. 16(b), where, since the object field does not diffuse over the maximum diffraction angles given as $\theta'_{x,y} = \sin^{-1} \lambda/(2\Delta_{x,y})$ in the x and y directions, the object field extends fully in region A and partially in region B. As a result, we adopt the criterion that the pupil position (i.e., the center of the pupil) should be at least inside region A. The minimum pupil distance can, therefore, be obtained from the simple geometrical analysis given below:

$$d_P \geq \frac{2x_{e,\max} + w_x}{2 \tan \theta'_x}, \qquad \frac{2y_{e,\max} + w_y}{2 \tan \theta'_y}, \qquad (14)$$

where $x_{e,\max}$, $y_{e,\max}$, and $w_{x,y}$ are the absolute values of the maximum pupil position and the lateral extents of the object space, respectively. In Figs. 13 and 14, where the lateral extents of the object space are $w_x = 1.3\,\text{cm}$ and $w_y = 0.6\,\text{cm}$, the minimum pupil distance obtained from Eq. (14) is approximately 17 cm. Thus, $d_P = 20\,\text{cm}$ was adopted for the numerical reconstruction.

6. Conclusion

Free-viewpoint images for self- and mutually occluded objects were obtained by using phase-shifting synthetic aperture digital holography. The capture of object waves using digital holography commonly suffers from narrowness of both the viewing zone and the visual field. In this report, the viewing zone is enlarged by extending the effective sensor size, using
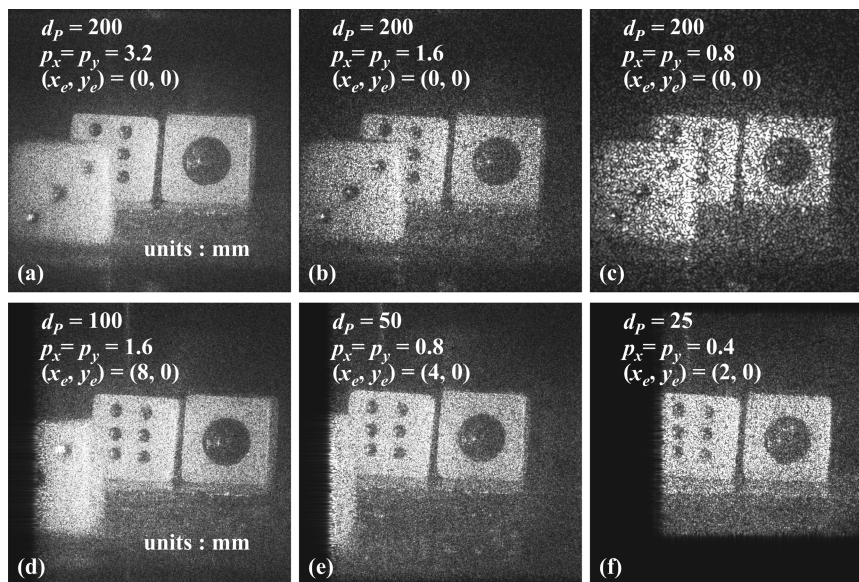

Fig. 16. Numerical reconstruction using different pupils: (a)–(c) Only the pupil size varies; (d)–(f) the pupil distance differs, but all pupils are placed in the same line of sight and have the same angle $\varphi_{x,y}$ as that used in Fig. 13.
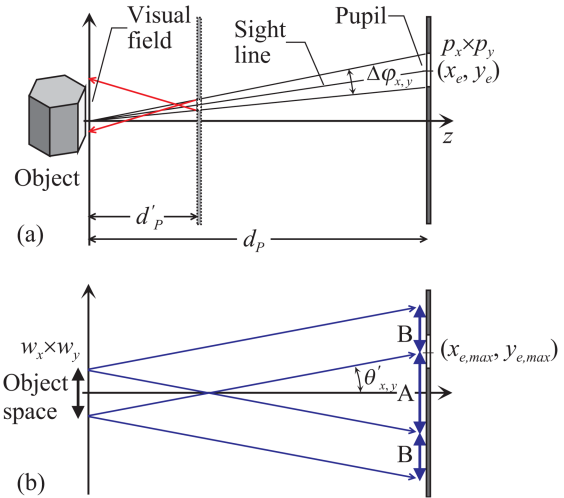
a synthetic aperture technique. A phase-shifting lensless Fourier setup and aliasing-free zone are also used to enlarge the visual field and to avoid aliasing errors caused by extending the sensor size.

Reconstruction of different perspectives is obtained by digital signal processing (DSP) of captured wave fields, involving a double numerical propagation and clipping the wave field by the pupil placed at a given viewpoint. In this method, a double fast Fourier transform is the computational complexity required for reconstructing an amplitude image from the base wave field.

Experimental results show that free-viewpoint images obtained from the proposed method are capable of reconstructing natural occlusion for both self- and mutually occluded objects. Free-focus images are a natural result in digital holography. This report shows that free-viewpoint images as well as free-focus images are also possible in digital holography. Various methods of DSP of light are expected in the future.

References

1. K. Matsushima, "Formulation of the rotational transformation of wave fields and their application to digital holograph," Appl. Opt. **47**, D110–D116 (2007).
2. L. Xu, X. Peng, J. Miao, and A. K. Asundi, "Studies of digital microscopic holography with applications to microstructure testing," Appl. Opt. **40**, 5046–5051 (2001).
3. Y. S. Hwang, S.-H. Hong, and B. Javidi, "Free view 3-D visualization of occluded objects by using computational synthetic aperture integral imaging," J. Display Technol. **3**, 64–70 (2007).
4. S.-H. Hong and B. Javidi, "Three-dimensional visualization of partially occluded objects using integral imaging," J. Disp. Technol. **1**, 354–359 (2005).
5. A. W. Lohmann, "Three-dimensional properties of wavefields," Optik (Jena) **51**, 105–117 (1978).
6. T. Hamano and M. Kitamura, "Computer-generated holograms for reconstructing multi-3-D images by space-division recording method," Proc. SPIE **3956**, 23–32 (2000).
7. K. Matsushima and A. Kondoh, "A wave optical algorithm for hidden-surface removal in digitally synthetic full-parallax holograms for three-dimensional objects," Proc. SPIE **5290**, 90–97 (2004).
8. A. Kondoh and K. Matsushima, "Hidden surface removal in full-parallax CGHs by silhouette approximation," Syst. Comput. Jpn. **38**, 53–61 (2004).
9. K. Matsushima, "Exact hidden-surface removal in digitally synthetic full-parallax holograms," Proc. SPIE **5742**, 25–32 (2005).
10. J. Maycock, C. P. McElhinney, B. M. Hennelly, T. J. Naughton, J. B. McDonald, and B. Javidi, "Reconstruction of partially occluded objects encoded in three-dimensional scenes by using digital holograms," Appl. Opt. **45**, 2975–2985 (2006).
11. R. Binet, J. Colineau, and J.-C. Lehureau, "Short-range synthetic aperture imaging at 633 nm by digital holography," Appl. Opt. **41**, 4775–4782 (2002).
12. V. Mico, Z. Zalevsky, P. García-Martínez, and J. García, "Synthetic aperture superresolution with multiple off-axis holograms," J. Opt. Soc. Am. A **23**, 3162–3170 (2006).
13. I. Yamaguchi and T. Zhang, "Phase-shifting digital holography," Opt. Lett. **22**, 1268–1270 (1997).
14. C. Wagner, S. Seebacher, W. Osten, and W. Jüptner, "Digital recording and numerical reconstruction of lensless fourier holograms in optical metrology," Appl. Opt. **38**, 4812–4820 (1999).
15. I. Yamaguchi, J. Kato, S. Ohta, and J. Mizuno, "Image formation in phase-shifting digital holography and applications to microscopy," Appl. Opt. **40**, 6177–6186 (2001).
16. J. W. Goodman, *Introduction to Fourier Optics*, 2nd ed. (McGraw-Hill, 1996), chap. 3.10.